

# Highly sensitive three-dimensional scanning triboelectric sensor for digital twin applications<sup>☆</sup>

Jiayue Zhang<sup>b,1,2</sup>, Shaixin Li<sup>a,c,1</sup>, Zhihao Zhao<sup>a,c,1,3</sup>, Yikui Gao<sup>a</sup>, Di Liu<sup>a,c</sup>, Jie Wang<sup>a,c,\*4</sup>, Zhong Lin Wang<sup>a,c,d,\*5</sup>

<sup>a</sup> Beijing Institute of Nanoenergy and Nanosystems, Chinese Academy of Sciences, Beijing 100083, PR China

<sup>b</sup> Department of Mechanical Engineering, Tsinghua University, Beijing 100084, PR China

<sup>c</sup> School of Nanoscience and Technology, University of Chinese Academy of Sciences, Beijing 100049, PR China

<sup>d</sup> School of Materials Science and Engineering, Georgia Institute of Technology, Atlanta, GA 30332, United States



## ARTICLE INFO

### Keywords:

Triboelectric nanogenerator  
Force sensor  
Three-dimensional scanning  
Digital twin  
Post-process

## ABSTRACT

Digital twin benefits for product designing, simulating, and troubleshooting. To obtain a more realistic digital model, it is crucial to accurately collect point could data in the complex environment affected by light, sound, and electromagnetic fields. In this paper, a three-dimensional (3D) scanning system is proposed to achieve distinguishing output and almost damage-free point cloud collection to the surface of objects. Thanks to the linearity between voltage signal and sliding displacement of sliding triboelectric nanogenerator (S-TENG), a self-powered point cloud collecting probe has been designed. More importantly, S-TENG probe generates high voltage with little friction force making it almost no damage to the contact surface of the sample object while scanning. To enormously improve the accuracy of the whole system, a productive post-processing system has been proposed to recognize and compensate for the noise and baseline drift errors caused by the surrounding environment. This system vigorously promotes the development of digital twin technology, contributing to intelligent manufacture, intelligent medical care, and cultural relics protection.

## 1. Introduction

Digital twins could be seen as the virtual replica of physical bodies, intended for bionic product design and simulation for medical application [1,2], historic works reconstruction and analysis for cultural inheritance [3], simulation and calculation for virtual reality (VR) and augmented reality (AR) [4], as well as metrology and quality inspection for intelligent manufacturing [5], as shown in Fig. 1a. Point cloud, acquired by three dimensional (3D) scanner, is the foundation of building digital models, playing a key role to realize digital twins [6,7]. Currently, plentiful researches have been carried out to obtain point

cloud based on computer vision technology [8,9]. This method has the advantage of no damage on the object surface, but the accuracy of the data is greatly affected by the environment conditions, such as dust and optical environment in the surroundings. Besides, the transparency, reflection intensity, surface roughness, and even the color of the sample are strictly restricted [10–12]. Another option, the contact scanning technology, utilizes its scanning probe to contact the sample with planned path, and records coordinates of the probe when valid signals received, as shown in Fig. 1b. This kind of scanner has higher accuracy and is less likely to be affected by the surrounding environment. The color, illumination, and transparency of the sample would not influence

\* Prof Zhong Lin Wang, an author on this paper, is the Editor-in-Chief of Nano Energy, but he had no involvement in the peer review process used to assess this work submitted to Nano Energy. This paper was assessed, and the corresponding peer review managed by Professor Chenguo Hu, also an Associate Editor in Nano Energy.

\* Corresponding author at: Beijing Institute of Nanoenergy and Nanosystems, Chinese Academy of Sciences, Beijing 100083, PR China.

E-mail addresses: [wangjie@binn.cas.cn](mailto:wangjie@binn.cas.cn) (J. Wang), [zhong.wang@mse.gatech.edu](mailto:zhong.wang@mse.gatech.edu) (Z.L. Wang).

<sup>1</sup> These authors contributed equally.

<sup>2</sup> ORCID: 0000-0002-0612-4800.

<sup>3</sup> ORCID: 0000-0001-5944-9687.

<sup>4</sup> ORCID: 0000-0003-4470-6171.

<sup>5</sup> ORCID: 0000-0002-5530-0380.

the scanning process either. Nevertheless, due to the configuration and principle of the commonly used piezoresistive or piezoelectric sensors, the contact scanner may damage the scanning surface of the object. Hence, performing 3D scanning with high accuracy without damaging the surface is a huge challenge.

Due to the scanning mechanism, it is difficult for non-contact sensors to avoid the shortcoming of being easily affected by the environment, while contact sensors can greatly reduce the damage to the surface of the object by choosing a pressure sensor with higher resolution, which is defined as the smallest change that can be achieved or measured. To simultaneously achieve high precision and low damage goals, a highly sensitive sensor, which means a sensor with distinguishing output and high resolution is required. Triboelectric nanogenerator (TENG) proposed in 2012 converts mechanical motion or deformation into electrical potential output due to contact electrification and electrostatic induction [13–16]. Compared with other sensors that can detect the action of contact, such as piezoresistive sensors, piezoelectric sensors,

etc., TENG-based sensors have a large voltage output and high resolution [17–19]. Besides, the output signals of the TENG-based sensor are closely related to the input mechanical behavior, which makes the post-analysis feasible [20–23]. Since the sensor converts the contact action between the probe and the object into electrical signals as an input to the whole system to realize perception, its transmission of electrical signals will be affected by the electromagnetic field in the surroundings during the scanning operation [24,25]. The higher resolution the sensor has, the more pronounced the disturbance to its electrical signals is, which will influence the final result. This leads to a difference between the electrical signals collected and the real electrical signal. Reducing this error can make the scan results closer to the real situation and further improve the accuracy. Research on how to reduce this error under this application has not received enough attention, though it is remarkably necessary.

In this paper, a 3D scanning system has been built up with a TENG-based sensor and an efficient post-processing system. A probe

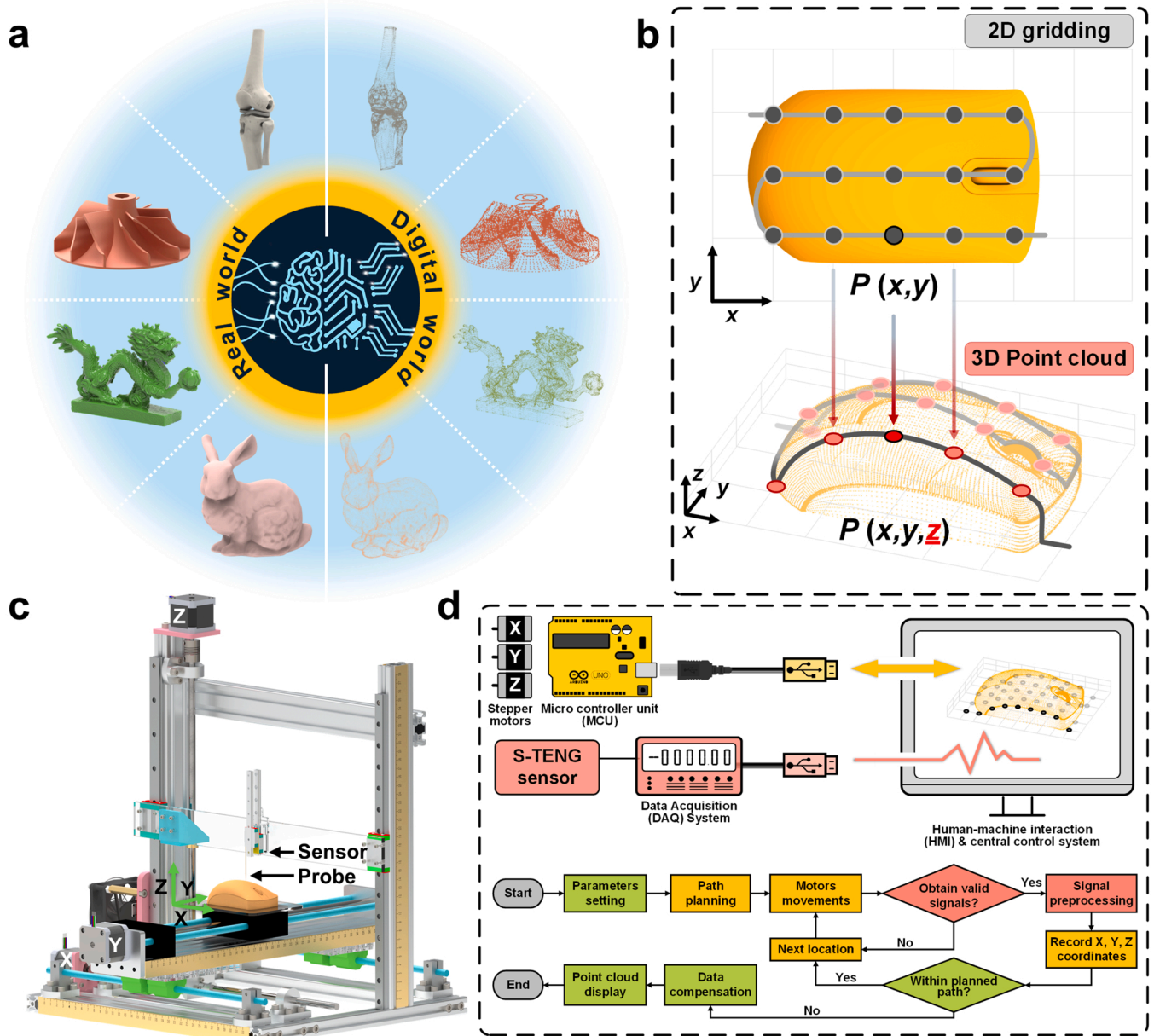


**Fig. 1.** Working principle of TENG-based 3D scanning system. (a) Schematic diagram of diverse items in the real world and digital world. (b) The overall plan of 3D scanning. (c) The hardware setup of TENG-based 3D scanning system. (d) Electronic systems of TENG-based 3D scanning system.

configuration equipped with the TENG-based sensor is designed, which could collect the point cloud with almost no damage on the scanning surface of objects. The post-processing algorithm embedded in this system hugely improves the consistency and stability of the output signals. Collected and modified by this system with high precision and low damage, two sets of resultant point clouds have been evaluated by comparing with the standard manufacturing mesh file and printing the reconstructed computer-aided design (CAD) files. The results show that the post-processing system greatly improves the accuracy of point cloud collection by around 30%. This work provides a new strategy for 3D scanning and contributes to promoting the development of digital twin technology.

## 2. Materials and methods

The output voltage signals of sensors were tested by the programmable electrometer (6514, Keithley Instruments model). The working status simulation test of various sensors in this experiment was achieved by a linear motor (TSMV120-1S, LinMot). The standard sample mouse in the experiment was fabricated with a 3D printer (FLASHFORGE GUIDER IIS).

The sliding triboelectric nanogenerator (S-TENG) sensor consists of two parts: the slider and the stator. For the slider, a mini block, with the size of 25 mm × 20 mm serves as the substrate. The block could move freely along the linear guide rail. A copper foil with the same size has been adhered onto it as one electrode. For the stator, a mini block, with the size of 25 mm × 20 mm serves as the substrate. The block is fixed on the rail. A copper foil with the same size has adhered onto it as another electrode, and a polytetrafluoroethylene (PTFE) film with the thickness of 0.05 mm with the same size is stuck onto the copper foil. Three identical acrylic holders cut with two rectangular holes keep the parallelism, distance, and contact force between the two contact surfaces. This 3D scanner system could be divided into two sections: the mechanical system and the electrical system. In the mechanical system, the frame is built by aluminum profiles with the overall dimensions of 370 mm × 420 mm × 420 mm, and three linear guide rails attached to it to achieve the movement. The effective stroke is 250 mm in x direction, 360 mm in y direction, and 340 mm in z direction. In the electrical system, movements in x, y, and z directions are achieved by stepper motors (Nema 17 stepper motor for x and y direction, and Nema 23 stepper motor for z direction). These motors are driven by an MCU (Arduino UNO with CNC shield V3 and three A4988 stepper drivers). Software (programmed with MATLAB) on a personal computer processes the voltage signals from the programmable electrometer (6514, Keithley Instruments model) and sends them to the MCU. The software on a personal computer (PC) communicates with the MCU through a serial port, and communicates with the master software of the electrometer through the virtual serial port.

## 3. Results and discussion

### 3.1. Working mechanism of the 3D scanning system

The 3D scanning system is a kind of mechatronics equipment, consisting of mechanical system and an electronic system. The mechanical system is composed of three orthogonal axes, mainly achieved by three linear motion modules (including motors, linear guide rail, and other necessary elements) and aluminum profiles, as shown in Fig. 1c. The sample to be scanned moves along x- and y-axis, and the scanning probe moves along z-axis. A sensor above the scanning probe is to sense the contact of the probe and the sample object. In the electronic system, as shown in Fig. 1d, a PC serves as a central controller, used for scanning parameters setting, human-machine interaction (HMI), overall feedback control of the movements, data compensation, and the results display. A microcontroller unit (MCU) is employed to plan the scanning path and drive the motors. A data acquisition (DAQ) system, incorporating

electrometer, analog to digital (A/D) converter, and programmable software, contributes to signal acquisition and preprocessing.

During the scanning system operation, the scanning system automatically divides the whole scanning area into several intervals and plans the scanning path, after the scanning parameters set (Fig. 1b). As the sample moves to locations on the planned path in sequence, the probe moves downwards until the sensor transmits a valid contact signal (Fig. 1c). Once there is a valid signal, the DAQ preprocesses and sends the signal to MCU, and the MCU records the current position of the motor Z. The coordinates of the sample surface are calculated based on the planned path and the collected z-axis information. With data compensation, point cloud of the sample surface is obtained. In the whole process, software on PC is responsible for signal monitoring and overall feedback control (Fig. 1d). More details about the software on PC are shown in Fig. S1 and Note S1.

The value of the resolution of the mechanical system is the minimum movement distance that can be driven by the motor. Since the movements of the mechanical system in x, y, and z directions are realized by the screw-slider module, the theoretical minimum value of the resolution of the scanning system are closely related to the lead of the lead screw and the resolution of the motor (Fig. S2). The theoretical minimum value of the resolution could be calculated as follows:

$$R_{min} = l \times r / 2\pi \quad (1)$$

where  $R_{min}$  is the theoretical minimum value of the resolution of the axis with the unit of millimeter,  $l$  is the lead of the lead screw with the unit of millimeter, and  $r$  is the step angle of the motor with the unit of radius.

### 3.2. Output performance of the TENG sensor

To determine the coordinates of the discrete points, it is vital to accurately sense the contact between the probe and the sample. To protect the sample surface, the contact force should be as small as possible, which means the sensor has to accurately catch the contact moment. Additionally, involving motors, MCU, and various electronic components, this electromechanical system introduces electromagnetic interference in signal reception, which is manifested as noise in signal data. Therefore, the judgment of contact signals has to eliminate the influence of noise. Besides, since numerous positions on the planned path waiting to be scanned, the sensor ought to have consistent performance.

The performances of four common force sensors have been tested and shown in Fig. 2. Piezoelectric ceramics could convert mechanical force into voltage signal output due to the piezoelectric effect and is a kind of self-powered sensor (Note S2) [26,27]. The electrification principle and test diagram are shown in Fig. 2a(i). The performance of a commercial piezoelectric ceramics sheet has been evaluated as shown in Fig. 2a(ii). The minimum sensing force, 0.1 N, is quite small, which means its force resolution is excellent. The voltage signal is perfectly linearly related to the external force. However, the sensitivity, defined as the slope of the curve, indicating how much the output changes as the input changes, of this piezoelectric ceramic sheet is 0.11 V/N, which is quite small. Under 7.4 N, the voltage output is only 1.07 V, which would be overwhelmed by noise. To increase the signal-to-noise ratio, larger pressure needs to be applied, and that introduces damage onto the scanned surface. To make the damage clearer, a plasticine experiment has been carried out in Fig. 2a(iii). Setting a voltage value threshold distinguishingly larger than the noise and driving the probe with the sensor moving downwards onto the plasticine, the damage on the surface is visualized (Video S1). The resistance of the strain gauge is accordingly changing with the mechanical deformation due to the strain effect (Note S3) [28]. To more accurately analyze the performance of a commercial strain gauge, a 10 kΩ resistor is matched in the circuit as shown in Fig. 2b(i). Since this sensor changes the voltage signals by changing its resistance in the measurement circuit, instead of generating

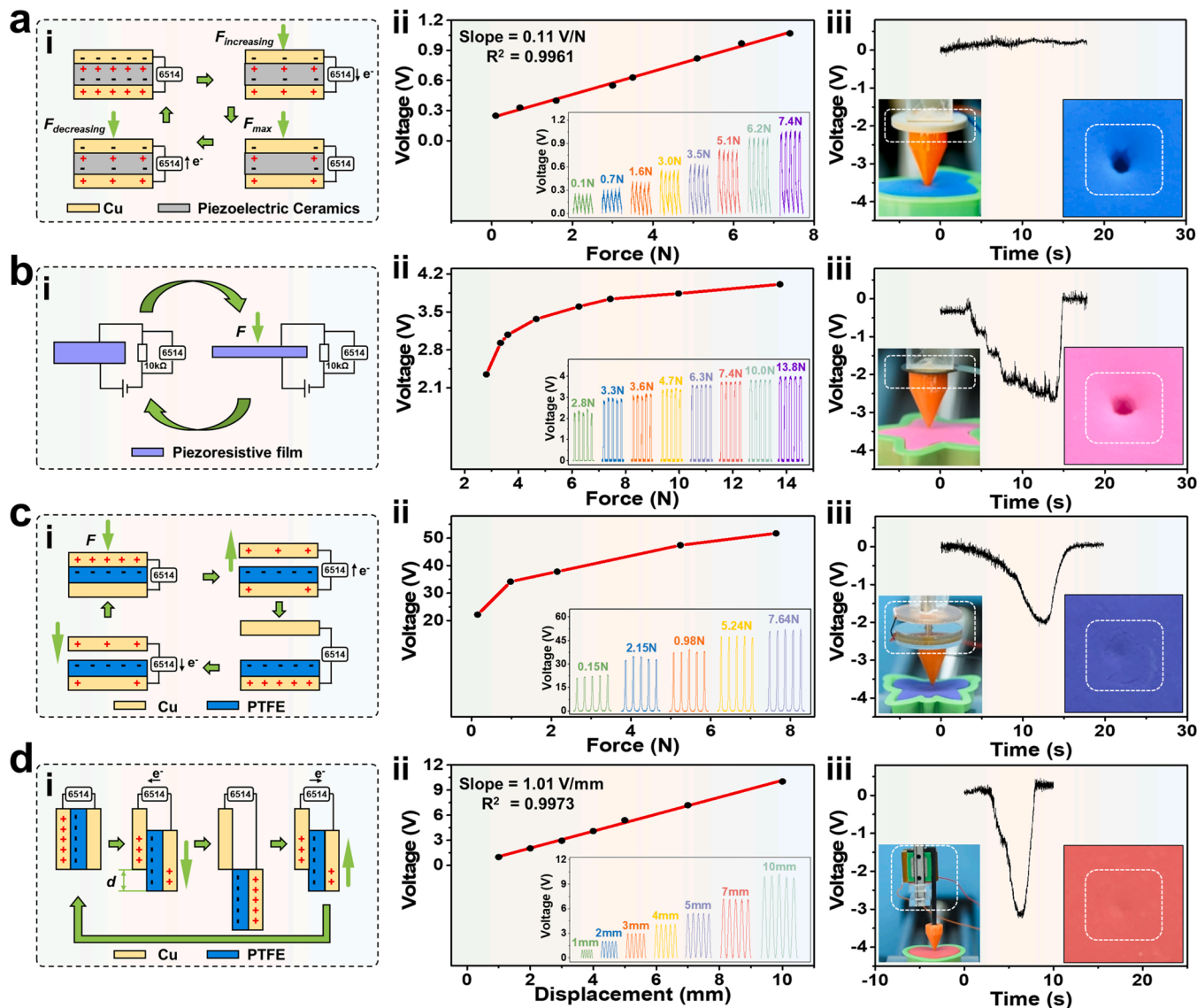


**Fig. 2.** Performance comparison of force sensors. (a) Piezoelectric ceramic sheet's information ((i) test diagram, (ii) the relation between force and voltage (the insert is raw voltage signal data under different forces), and (iii) plasticine visualization experiment data (the insert is the experiment setting and the force effect on plasticine)). (b) Strain gauge's information ((i) test diagram, (ii) the relation between force and voltage (the insert is raw voltage signal data under different forces), and (iii) plasticine visualization experiment data (the insert is the experiment setting and the force effect on plasticine)). (c) CS-TENG sensor's information ((i) test diagram, (ii) the relation between force and voltage (the insert is raw voltage signal data under different forces), and (iii) plasticine visualization experiment data (the insert is the experiment setting and the force effect on plasticine)). (d) S-TENG sensor's information ((i) test diagram, (ii) the relation between force and voltage (the insert is raw voltage signal data under different displacements), and (iii) plasticine visualization experiment data (the insert is the experiment setting and the force effect on plasticine)).

voltage signals, it is less interfered with by the environmental electromagnetic field. However, this feature also causes a high latency. Besides, the minimum measurable force is 2.81 N, which is a relatively large value (Fig. 2b(ii)), leading to the damage on the sample surface, which is visualized in Fig. 2b(iii). Another option is the contact-separation model TENG (CS-TENG) based on the contact electrification effect (Note S4). Contacting with the sample, as the force on the probe increases, the effective contact area of the electrode and dielectric increases, leading to an increase in voltage signal [29–31]. This kind of sensor has high resolution, resulting in almost no damage on the contact surface (Fig. 2c(ii) and c(iii)). However, the configuration of CS-TENG makes it impossible to have large deformations, introducing difficulties and limitations to the scanning system design and control algorithm.

Supplementary material related to this article can be found online at doi:10.1016/j.nanoen.2022.107198.

The sensors above could not meet the requirements of this application. The deformable displacement of the piezoelectric ceramic sheet, strain gauge, and CS-TENG is not large enough, which may lead to damage to the sample surface. The mechanism of S-TENG (Note S5) is shown in Fig. 2d(i) [32,33]. PTFE and copper are used as material pairs for electrification. Due to the contact electrification effect and different electronegativity of PTFE and copper, they obtain equal negative and positive charges respectively when they contact each other. After the contact moment, due to the electrostatic induction, the electron transfers from the slider electrode (the right one shown in Fig. 2d(i)) to the stator electrode (the left one shown in Fig. 2d(i)) to balance the potential difference during the slider moves downwards, because the valid area decreases. The electrons move back to the stator electrode when the slider moves back, while the valid area increases. Thus, an alternating voltage can be generated by S-TENG. Generally, it takes some time to

saturate the surface charge, though saturation can be reached very quickly for S-TENG. To avoid the influence of it on the measurement precision, the slider of the S-TENG sensor would be moved back and forth a few times to reach the saturation state before the scanning process. During the measurement, the surface charge density will remain saturated due to the surface friction between the dielectric surface and the electrode surface. It is worth noting that the output voltage is positively correlated to the contacting area of PTFE and the copper, which in this work depends on the sliding distance, considering the probe movement along  $z$ -axis.

Shown in Fig. 2d(ii), the sensitivity of this S-TENG sensor is  $1.01 \text{ V/mm}$ , which could be improved by increasing the size of the sensor, etching microstructure on the surface of PTFE film, and selecting other friction material pairs with better electrification properties. In addition, the excellent linearity of the sliding distance and the output voltage signals helps to data compensation for baseline drift due to mechanical structure or electromagnetic noise. Compared with the other sensors, the

S-TENG sensor leads to quite low damage to the sample surface. The force driving the probe is about  $0.23 \text{ N}$  (Video S2). Although it is a little larger than that of CS-TENG, it is acceptable and the configuration of S-TENG leaves a larger fault tolerance for the controlling system, resulting in almost no damage to the measured surface (Fig. 2d(iii)). Details of the sensors and experiment settings are shown in Fig. S3.

Supplementary material related to this article can be found online at doi:10.1016/j.nanoen.2022.107198.

### 3.3. Data post-processing system

During 3D scanning operation, the complex electromagnetic fields in the surrounding environment lead to two main issues in voltage signal data: noise and baseline drift. To eliminate the influence of noise, a threshold has been set before scanning. With this threshold, effective voltage signal and ineffective noise could be distinguished, and possible misjudgment could be circumvented.

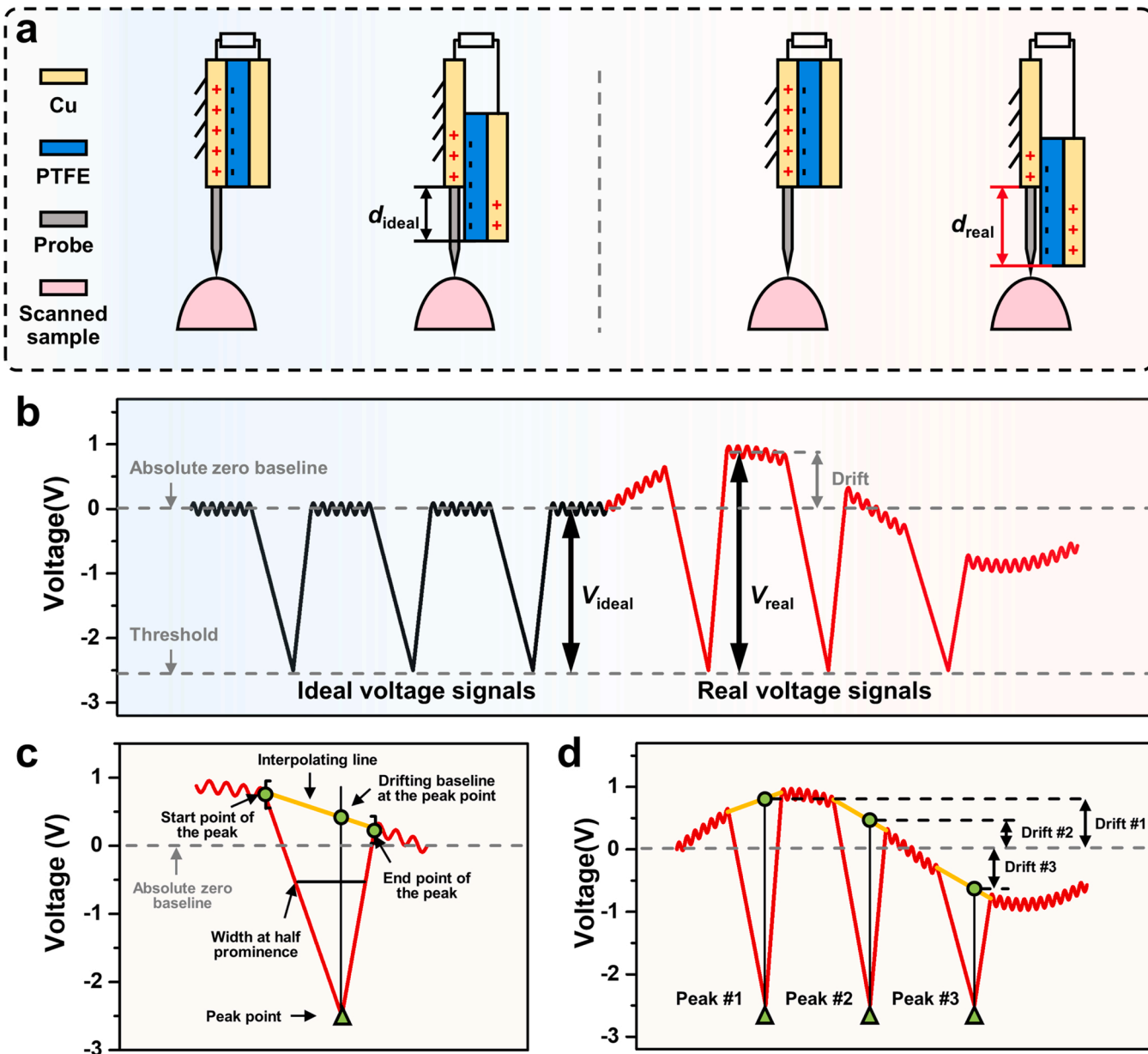


**Fig. 3.** Diagram of baseline drift situation and the data compensation strategy. (a) S-TENG sensor operates in an ideal situation and a real situation. (b) The voltage data under ideal situation and real situation. (c) Interpolation between the start and the end point of each peak. (d) Baseline drift values for every peak of the voltage signals.

The drift of baseline is a more difficult affair. As shown in Fig. 3a and b, in an ideal situation, from the moment the probe touches the sample to the moment the effective signal is received by the system, the output voltage difference of the sensor is a constant value  $V_{ideal}$ , and the sliding distance of the corresponding sensor electrodes is also a constant value  $d_{ideal}$ . However, due to baseline drift, for example, upward drift, the sensor needs to output a larger voltage  $V_{real}$  to reach the threshold set, so the sliding distance  $d_{real}$  of its corresponding electrodes also increases, which causes inaccuracy in coordinates collection of points.

It is difficult to set an adaptive threshold. Since the drift and noises are irregular, the storage and analysis of all the history data are needed to predict the future baseline and set the real-time and adaptive threshold. However, while there is no enough data to forecast the threshold for the first few sampling points, it is also a heavy burden for computer memory with more and more data collected. As the number of calculations increases, the response time becomes longer and longer, which results in delayed feedback and inaccurate results.

Hence, a post-processing system has been proposed. In this scanning system, each sampling point is mapped to a peak in the voltage signal curve. For each peak, as shown in Fig. 3c, the location of the peak point, the start point of the peak, and the end point of the peak have been found. Interpolated between the start point and the end point of the peak, the baseline position for the peak could be found. According to the voltage-displacement linear relationship measured in Fig. 2d(ii), conversion from voltage baseline drift to the electrode displacement has been done. The post-process and compensation finished with assigning the baseline data to each sampling point. Since this post-processing strategy is based on the voltage data itself, it is adaptive. The post-processing system finds and calculates the baseline drift for each sampling point concerning the local peaks, instead of an absolute value, avoiding misjudgments. Besides, this post-processing strategy could be widely used in different operating conditions, especially for those sensor signals irregularly drifting scenarios. For any operation environment, as the approximate noise is known, the threshold could be set to a larger value than the noise value. Similar strategies could be occupied to find the difference between the measured value and the actual value, and make the data compensation. The applications of this scheme in the actual signal curves are shown in Figs. S4 and S5.

### 3.4. Evaluation of the 3D scanning system

After digitally modeled, a mouse is manufactured by a 3D printer. The range of sampling is 70 mm and 40 mm in  $x$  direction and  $y$  direction respectively. Hence, the sampling zone is set to be 75 mm  $\times$  75 mm in  $xy$ -plane. In this work, a lead screw with an 8 mm lead was used to control the movement of the  $x$ -axis and  $y$ -axis, and a lead screw with the lead of 2 mm was used to control the movement of the  $z$ -axis. The resolution of the driven motors under full step mode is  $0.01\pi$ . The theoretical minimum value of the resolution of  $x$ -axis and  $y$ -axis is 0.04 mm, while that of  $z$ -axis is 0.01 mm. Although setting the value of the scan step to be the minimum value of the resolution can achieve greater scan accuracy, it would occupy a long scanning time. Moreover, the acceleration and deceleration process during the motors operation may introduce inaccuracy into the system due to the small step distances. Therefore, comprehensively considering working hours and measurement accuracy requirements, the step distance in  $x$  and  $y$  directions are set to be 3 mm, and that in  $z$  direction is set to be 1 mm, which means the value of the resolution in  $x$  and  $y$  directions is 3 mm, and in  $z$  direction is 1 mm. The setting of the scanning system and the evaluation flow are shown in Fig. 4a and c, respectively.

Collected 256 valid points, the post-processing system has been engaged to find the peaks of the voltage signal data correspondingly. With the start point, end point, and peak point of each peak, the system has interpolated between the start and the end point to find the baseline drift for each peak. After allocating the matching value of distance converted according to 1.01 V/mm to each sampling point, and

removing the grounding points, the final point cloud has been obtained. The point cloud constructed from raw data and processed data is shown in Fig. 4b(i). The post-processing data of the sample mouse is shown in Fig. S4.

Reconstructing the measured surface by interpolating the point cloud of raw data and processed data, from Fig. 4b(ii) to Fig. 4b(iii), it is obvious that the surface is modified by the post-processing system. In Fig. 4b(iv) and Fig. 4b(v), both the raw point cloud and modified point cloud have been compared with the standard mesh STL file. The histograms of the distance between the point cloud and the mesh are shown in Fig. 4b(vi) and Fig. 4b(vii). The histograms are fitted with Gauss distribution to show the effect of the modification. The distance between the CAD model mesh for manufacturing and each point in the point cloud data set is defined as the evaluation indicator. Based on the raw data collected by the scanning system, the mean value of the unsigned distance between the point cloud and the mesh is 0.43 mm, the standard deviation is 0.33 mm, and the maximum distance is 1.91 mm. After post-processed, the mean distance is 0.30 mm, decreased by 30.23%, the standard deviation is 0.23 mm, decreased by 30.30%, and the maximum distance is 1.51 mm decreased by 20.94%. The reconstructed model has been 3D printed and compared with the original 3D printed model (Fig. 4d(i)). The whole process from the data collection to the printing of the reconstructed digital model has been recorded in Video S3.

Furthermore, to test the performance of the scanning system on surfaces with different characteristics, an item with a bumpy surface, which looks like a wave, has also been scanned (Fig. 4d(ii)). The experiment setting, post-processing data, and more comparison diagrams of this wave sample are shown in Figs. S4, S5, and Note S6. In this paper, the scan path grids are all squares with 3 mm intervals, therefore, it is poorly fitted to non-straight edges such as circles and arcs, which could be observed in Fig. 4d. Reducing the interval spacing, improving the path planning algorithm, and designing more adaptive gridding patterns (inclined grids and polar grids described in Fig. S6 and Note S7 are two possible solutions) would reform this problem. In the future, for objects with more complex geometric configurations, a combination of multiple grids can be programmed to achieve higher-precision data collection, especially for points on the edges of objects. To scan lateral surfaces, a probe that can move along the vertical linear guide rail standing next to the tray will cooperate with the rotating tray to collect the point clouds on the side surface of the object (Fig. S7a). Multi-dimensional sensing requirements can be achieved by appropriately arranging multiple sensors. Further, to increase the scanning efficiency, a probe array could be integrated into this scanning system (Fig. S7b). Apart from serving as an operation platform, the scanning system presented in this paper could also act as an end effector on robots for detecting and measuring applications, promoting the development of artificial intelligence (Fig. S7c, d and Note S8).

### 4. Conclusions

In summary, a 3D scanning system with an S-TENG sensor has been proposed in this paper. The S-TENG sensor has excellent performance on low damage and high output and the post-processing system enormously improves the accuracy of the whole system. Comparing the raw point cloud of the sample mouse collected by the scanning system with the original digital model, the mean distance is 0.43 mm with a standard deviation of 0.33 mm. With post-process, the mean distance decreased by 30.23%, and the standard deviation (mainly comes from the mechanical system setting and the sample manufacturing) decreased by 30.30%. For irregular noise and baseline drift, the simple post-processing scheme proposed in this paper works well, and it could also be used to correct signal errors of other sensors in the future, especially for those scenarios where difficult to build physical models or machine learning models for preprocessing. To achieve higher accuracy, a more advanced 3D printer would be employed to manufacture the standard sample, and a more precise motor, more stable frame structure,

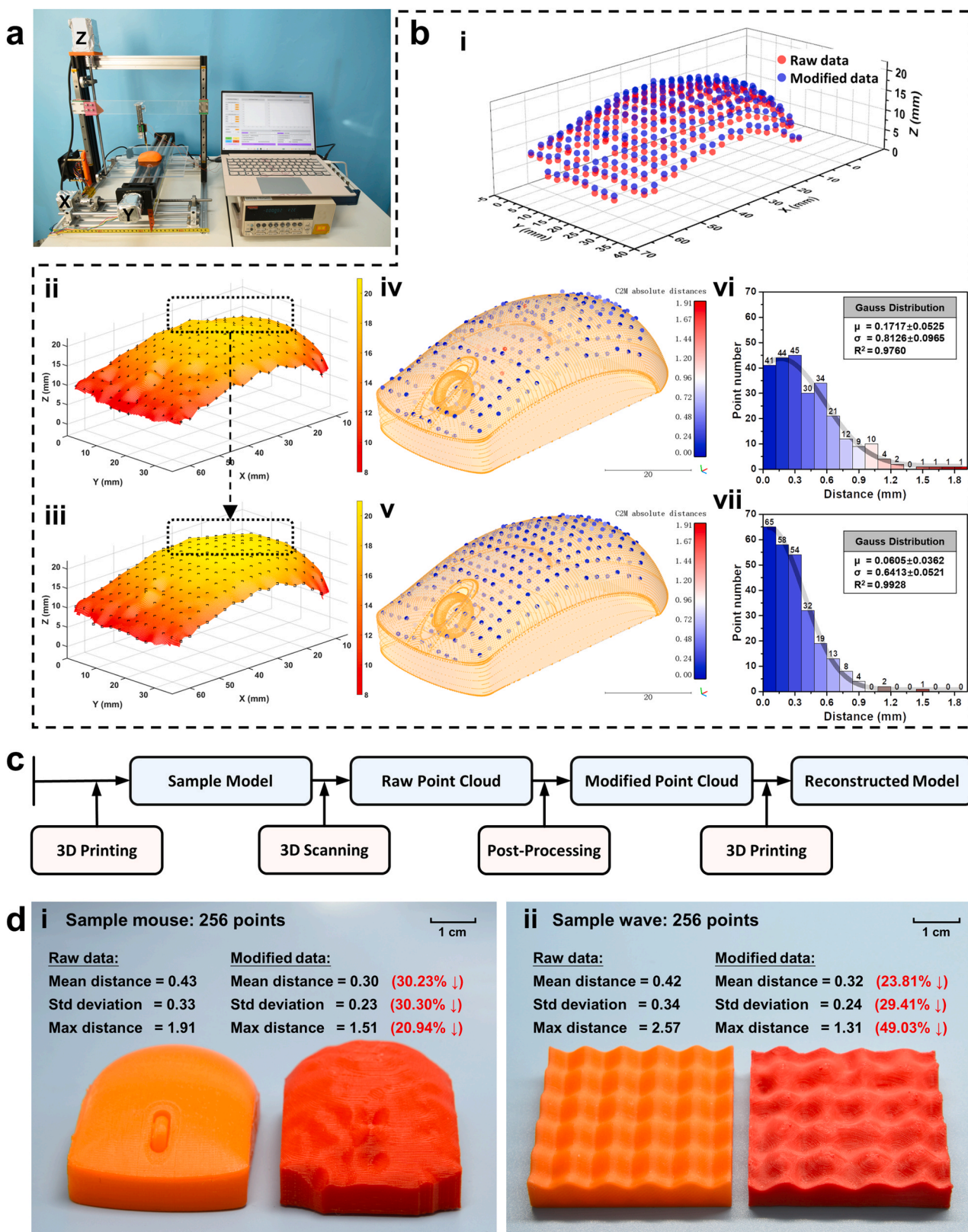


**Fig. 4.** Experimental setup and results. (a) Experimental setup. (b) The experimental results of point cloud comparison. ((i) the point cloud of raw data and modified data, (ii) the reconstructed surface of the raw point cloud, (iii) the reconstructed surface of the modified point cloud, (iv) the distance between the raw point cloud and the standard sample mesh, (v) the distance between the modified point cloud and the standard sample mesh, and (vi) the histogram of the distance between the raw point cloud and the mesh fitted with Gauss distribution, and (vii) the histogram of the distance between the modified point cloud and the mesh fitted with Gauss distribution). (c) Flow chart of the evaluation process. (d) The experimental results of 3D model comparison ((i) comparison of the original and reconstructed model of the sample mouse, (ii) comparison of the original model and reconstructed model of sample wave).

more reasonable assembly process, smaller stepping distance, and slower stepping speed should be achieved in the future. To have a better theoretical resolution, the lead screw with a smaller lead and the motor with a higher resolution could be selected. Additionally, the step distance could be set smaller to achieve a better practical resolution. The scanning accuracy could be further improved through the optimization of algorithms and scanning gridding solutions for objects with complex edges. The detection configuration implemented and proposed in this paper could be applied to industrial applications. This technology will greatly promote the development and application of digital twin technology.

### CRediT authorship contribution statement

**Jiayue Zhang:** Conceptualization, Methodology, Software, Supervision, Writing – original draft. **Shaixin Li:** Conceptualization, Methodology, Investigation, Supervision, Writing – review & editing. **Zhihao Zhao:** Investigation, Writing – review & editing, Supervision. **Yikui Gao:** Investigation. **Di Liu:** Investigation. **Jie Wang:** Conceptualization, Supervision. **Zhong Lin Wang:** Supervision.

### Declaration of Competing Interest

The authors declare that they have no known competing financial interests or personal relationships that could have appeared to influence the work reported in this paper.

### Acknowledgments

The authors acknowledge the financial support of the National Key R & D Project from Minister of Science and Technology (2021YFA1201602), the National Nature Science Foundation of China (61774016, 21773009, 22109013 and U21A20147), the China Postdoctoral Science Foundation (2021M703172), and the Fundamental Research Funds for the Central Universities (E1E46802).

### Author contributions

J.Z., S.L., and J.W. conceived the idea. S.L. designed and carried out the sensors and scanning experiments. J.Z. designed the mechanical structure and programmed for the control software. Z.Z., Y.G., and D.L. helped with the experiments. J.Z. drafted the manuscript. J.Z., S.L., Z.Z., J.W., and Z.L.W. supervised this work. All the authors discussed the results and commented on the manuscript.

### Appendix A. Supplementary material

Supplementary data associated with this article can be found in the online version at [doi:10.1016/j.nanoen.2022.107198](https://doi.org/10.1016/j.nanoen.2022.107198).

### References

- [1] J. Annese, N.M. Schenker-Ahmed, H. Bartsch, P. Maechler, C. Sheh, N. Thomas, J. Kayano, A. Ghatan, N. Bresler, M.P. Frosch, Postmortem examination of patient HM's brain based on histological sectioning and digital 3D reconstruction, *Nat. Commun.* 5 (2014) 1–9.
- [2] Y. Shi, F. Wang, J. Tian, S. Li, E. Fu, J. Nie, R. Lei, Y. Ding, X. Chen, Z.L. Wang, Self-powered electro-tactile system for virtual tactile experiences, *Sci. Adv.* 7 (2021) eabe2943.
- [3] X. Wei, D. Weng, Y. Liu, Y. Wang, A tour guiding system of historical relics based on augmented reality, in: Proceedings of the 2016 IEEE Virtual Reality (VR), IEEE, 2016, pp. 307–308.
- [4] T. Jin, Z. Sun, L. Li, Q. Zhang, M. Zhu, Z. Zhang, G. Yuan, T. Chen, Y. Tian, X. Hou, Triboelectric nanogenerator sensors for soft robotics aiming at digital twin applications, *Nat. Commun.* 11 (2020) 1–12.
- [5] Y. Xu, S. Joseph, P. Karamched, K. Fox, D. Rugg, F.P. Dunne, D. Dye, Predicting dwell fatigue life in titanium alloys using modelling and experiment, *Nat. Commun.* 11 (2020) 1–13.
- [6] W. Li, C. Pan, R. Zhang, J. Ren, Y. Ma, J. Fang, F. Yan, Q. Geng, X. Huang, H. Gong, AADS: augmented autonomous driving simulation using data-driven algorithms, *Sci. Robot.* 4 (2019) 1–12.
- [7] J. Tachella, Y. Altmann, N. Mellado, A. McCarthy, R. Tobin, G.S. Buller, J.-Y. Tourneret, S. McLaughlin, Real-time 3D reconstruction from single-photon lidar data using plug-and-play point cloud denoisers, *Nat. Commun.* 10 (2019) 1–6.
- [8] F. Ficuciello, A. Migliozzi, G. Laudante, P. Falco, B. Siciliano, Vision-based grasp learning of an anthropomorphic hand-arm system in a synergy-based control framework, *Sci. Robot.* 4 (2019) 1–11.
- [9] M.-J. Sun, M.P. Edgar, G.M. Gibson, B. Sun, N. Radwell, R. Lamb, M.J. Padgett, Single-pixel three-dimensional imaging with time-based depth resolution, *Nat. Commun.* 7 (2016) 1–6.
- [10] P. Rehain, Y.M. Sua, S. Zhu, I. Dickson, B. Muthuswamy, J. Ramanathan, A. Shahverdi, Y.-P. Huang, Noise-tolerant single photon sensitive three-dimensional imager, *Nat. Commun.* 11 (2020) 1–7.
- [11] R. Chen, S. Han, J. Xu, H. Su, Visibility-aware point-based multi-view stereo network, *IEEE Trans. Pattern Anal. Mach. Intell.* 43 (2020) 3695–3708.
- [12] L.S. Wilk, G.J. Edelman, M. Roos, M. Clerkx, I. Dijkman, J.V. Melgar, R.-J. Oostra, M.C. Aalders, Individualised and non-contact post-mortem interval determination of human bodies using visible and thermal 3D imaging, *Nat. Commun.* 12 (2021) 1–10.
- [13] F.-R. Fan, Z.-Q. Tian, Z.L. Wang, Flexible triboelectric generator, *Nano Energy* 1 (2012) 328–334.
- [14] Z.L. Wang, Triboelectric nanogenerators as new energy technology for self-powered systems and as active mechanical and chemical sensors, *ACS Nano* 7 (2013) 9533–9557.
- [15] Z.L. Wang, J. Chen, L. Lin, Progress in triboelectric nanogenerators as a new energy technology and self-powered sensors, *Energy Environ. Sci.* 8 (2015) 2250–2282.
- [16] Z.L. Wang, Triboelectric nanogenerators as new energy technology and self-powered sensors—principles, problems and perspectives, *Faraday Discuss.* 176 (2015) 447–458.
- [17] Z.L. Wang, Triboelectric nanogenerator (TENG)—sparking an energy and sensor revolution, *Adv. Energy Mater.* 10 (2020), 2000137.
- [18] Z. Lin, J. Chen, X. Li, Z. Zhou, K. Meng, W. Wei, J. Yang, Z.L. Wang, Triboelectric nanogenerator enabled body sensor network for self-powered human heart-rate monitoring, *ACS Nano* 11 (2017) 8830–8837.
- [19] Q. Zhou, J. Pan, S. Deng, F. Xia, T. Kim, Triboelectric nanogenerator-based sensor systems for chemical or biological detection, *Adv. Mater.* 33 (2021), 2008276.
- [20] S.W. Chen, X. Cao, N. Wang, L. Ma, H.R. Zhu, M. Willander, Y. Jie, Z.L. Wang, An ultrathin flexible single-electrode triboelectric-nanogenerator for mechanical energy harvesting and instantaneous force sensing, *Adv. Energy Mater.* 7 (2017), 1601255.
- [21] Y. Yang, H. Zhang, J. Chen, Q. Jing, Y.S. Zhou, X. Wen, Z.L. Wang, Single-electrode-based sliding triboelectric nanogenerator for self-powered displacement vector sensor system, *ACS Nano* 7 (2013) 7342–7351.
- [22] X. Yin, D. Liu, L. Zhou, X. Li, G. Xu, L. Liu, S. Li, C. Zhang, J. Wang, Z.L. Wang, A motion vector sensor via direct-current Triboelectric Nanogenerator, *Adv. Funct. Mater.* 30 (2020), 2002547.
- [23] S. Li, D. Liu, Z. Zhao, L. Zhou, X. Yin, X. Li, Y. Gao, C. Zhang, Q. Zhang, J. Wang, A fully self-powered vibration monitoring system driven by dual-mode triboelectric nanogenerators, *ACS Nano* 14 (2020) 2475–2482.
- [24] F. Yi, Z. Zhang, Z. Kang, Q. Liao, Y. Zhang, Recent advances in triboelectric nanogenerator-based health monitoring, *Adv. Funct. Mater.* 29 (2019), 1808849.
- [25] J. An, P. Chen, Z. Wang, A. Berbille, H. Pang, Y. Jiang, T. Jiang, Z.L. Wang, Biomimetic hairy whiskers for robotic skin tactility, *Adv. Mater.* 33 (2021), 2101891.
- [26] Z.L. Wang, J. Song, Piezoelectric nanogenerators based on zinc oxide nanowire arrays, *Science* 312 (2006) 242–246.
- [27] Z.L. Wang, On Maxwell's displacement current for energy and sensors: the origin of nanogenerators, *Mater. Today* 20 (2017) 74–82.
- [28] A. Rowe, A. Donoso-Barrera, C. Renner, S. Arscott, Giant room-temperature piezoresistance in a metal-silicon hybrid structure, *Phys. Rev. Lett.* 100 (2008), 145501.
- [29] G. Zhu, Z.-H. Lin, Q. Jing, P. Bai, C. Pan, Y. Yang, Y. Zhou, Z.L. Wang, Toward large-scale energy harvesting by a nanoparticle-enhanced triboelectric nanogenerator, *Nano Lett.* 13 (2013) 847–853.
- [30] S. Niu, S. Wang, L. Lin, Y. Liu, Y.S. Zhou, Y. Hu, Z.L. Wang, Theoretical study of contact-mode triboelectric nanogenerators as an effective power source, *Energy Environ. Sci.* 6 (2013) 3576–3583.
- [31] S. Niu, Z.L. Wang, Theoretical systems of triboelectric nanogenerators, *Nano Energy* 14 (2015) 161–192.
- [32] S. Wang, L. Lin, Y. Xie, Q. Jing, S. Niu, Z.L. Wang, Sliding-trioboelectric nanogenerators based on in-plane charge-separation mechanism, *Nano Lett.* 13 (2013) 2226–2233.
- [33] S. Niu, Y. Liu, S. Wang, L. Lin, Y.S. Zhou, Y. Hu, Z.L. Wang, Theory of sliding-mode triboelectric nanogenerators, *Adv. Mater.* 25 (2013) 6184–6193.